The Astrophysical Journal, 691:1042–1049, 2009 February 1 doi:10.1088/0004-637X/691/2/1042

NEAR-INFRARED [Fe II] AND H_2 LINE OBSERVATIONS OF THE SUPERNOVA REMNANT 3C 396: PROBING THE PRESUPERNOVA CIRCUMSTELLAR MATERIALS

Ho-Gyu Lee[1,2], Dae-Sik Moon[3], Bon-Chul Koo[1], Jae-Joon Lee[4], and Keith Matthews[5]
[1] Department of Physics and Astronomy, Seoul National University, Seoul, 151-742 Korea; hglee@astro.snu.ac.kr and koo@astrohi.snu.ac.kr
[2] Astrophysical Research Center for the Structure and Evolution of the Cosmos, Sejong University, Seoul 143-747, Korea
[3] Department of Astronomy and Astrophysics, University of Toronto, Toronto, ON M5S 3H4, Canada; moon@astro.utoronto.ca
[4] Department of Astronomy and Astrophysics, Pennsylvania State University, University Park, PA 16802, USA; lee@astro.psu.edu
[5] Division of Physics, Mathematics and Astronomy, California Institute of Technology, Pasadena, CA 91125, USA; kym@caltech.edu
Received 2008 July 13; accepted 2008 September 30; published 2009 January 28

ABSTRACT

We present the results of near-infrared [Fe II] and H_2 line imaging and spectroscopic observations of the supernova remnant 3C 396 using the Palomar 5 m Hale telescope. We detect long, filamentary [Fe II] emission delineating the inner edge of the radio emission in the western boundary of the remnant in imaging observations, together with a bright [Fe II] emission clump close to the remnant center. There appears to be faint, diffuse [Fe II] emission between the central clump and the western filamentary emission. The spectroscopic observations determine the expansion velocity of the central clump to be $\sim$ 56 km s^{-1}. This is far smaller than the expansion velocity of 3C 396 obtained from X-ray observations, implying the inhomogeneity of the ambient medium. The electron number density of the [Fe II] emission gas is $\leqslant$ 2000 cm^{-3}. The H_2 line emission, on the other hand, lies slightly outside the filamentary [Fe II] emission in the western boundary, and forms a rather straight filament. We suggest that the [Fe II] emission represents dense clumps in the wind material from the red supergiant phase of a Type IIL/b progenitor of 3C 396, which have been swept up by the supernova remnant shocks. The H_2 emission may represent either the boundary of a wind bubble produced during the main-sequence phase of the progenitor or molecular clumps left over inside the bubble. We propose that the near-infrared [Fe II] and H_2 emission observed in several supernova remnants of Type IIL/b SNe likely have the same origin.

Key words: circumstellar matter – infrared: ISM – ISM: individual (3C 396) – shock waves – supernova remnants

1. INTRODUCTION

The near-infrared (NIR) [Fe II] lines are useful tools for studying the radiative shocks of supernova remnants (SNRs). The increased abundance of gas phase iron by shock-induced sputtering of the dust grains and/or the creation of an extensive partially ionized zone by shock heating can substantially enhance the [Fe II] emission (e.g., Greenhouse 1991; Mouri et al. 2000). This, together with less severe extinction effects than the optical and the recent advents of NIR imaging cameras covering sufficiently wide fields (e.g., $\geqslant 5'$), can potentially make the observations of the NIR [Fe II] lines a very competitive and efficient way to study the radiative shocks of SNRs, especially in the Galactic plane where the extinction is usually large.

A good example is the young core-collapse SNR G11.2−0.3 where we recently found the brightest NIR [Fe II] emission of all known SNRs using the Wide-Field Infrared Camera (WIRC) aboard the Palomar 5 m telescope (Koo et al. 2007). Besides G11.2−0.3, a few other SNRs—such as RCW 103 (Oliva et al. 1999), 3C 391 (Reach et al. 2002), W44 (Reach et al. 2005), and W49B (Keohane et al. 2007)—have been detected in the NIR [Fe II] line emission.[6] Note that all these SNRs have a core-collapse nature and, except for W44, all of them are relatively young SNRs. Interestingly, in addition to the [Fe II] lines, NIR H_2 emission of shocked molecular gas has been detected from all these SNRs. The H_2 emission is distributed close to, but slightly outside, the [Fe II] emission from the center of the SNRs (e.g., Oliva et al. 1990; Keohane et al. 2007; Koo et al. 2007), which is opposite to the standard picture of the molecular shocks where molecules form in the downstream behind a recombination region. This apparent pattern of positional "reversal" between the [Fe II] and H_2 emission may have important clues to understanding the presupernova environment of SNRs, calling for more systematic investigation of the [Fe II] and H_2 emission together in (young) core-collapse SNRs.

In this paper we present the NIR imaging and spectroscopic observations of [Fe II] and H_2 lines from another core-collapse SNR 3C 396 (also known as G39.2–0.3). In radio 3C 396 is a shell-type SNR of $\sim 8' \times 6'$ size (Anderson & Rudnick 1993) composed of multiple elliptical arcs and filaments (Figure 1), with a thick, half ring-like feature in the west. The *Advanced Satellite for Cosmology and Astrophysics* (*ASCA*) X-ray observation revealed the existence of a pulsar wind nebula within a thermal X-ray shell (Harrus & Slane 1999), and the former was later resolved by *Chandra*, although no X-ray pulsation was detected (Olbert et al. 2003). Recently *Spitzer* detected bright mid-IR emission from this SNR along its western boundary in the radio (Lee 2005; Reach et al. 2006). The mid-IR emission is filamentary, and is prominent in the 4.5 and 5.8 μm bands. If the origin of the mid-IR emission is ionic and molecular lines as suggested (Lee 2005; Reach et al. 2006), we expect the existence of the corresponding NIR emission of the [Fe II] line at 1.64 μm and H_2 line at 2.12 μm from this SNR, which motivated our observations presented in this paper. The distance to 3C 396 is rather uncertain; however, most of the previous observations of H and OH indicate that it is beyond the tangential point at 6.6 kpc, and possibly at 9.6 kpc (Caswell et al. 1975; Becker & Helfand 1987; Green 1989). In this paper, we adopt the distance of 8.5 kpc determined on the basis of the velocity of a nearby molecular cloud in 3C 396 (see Section 4). We organize this

[6] Here we only consider [Fe II] emission from the radiative SNR shocks, excluding [Fe II] emission from the supernova ejecta (e.g., D.-S. Moon et al. 2009, in preparation).

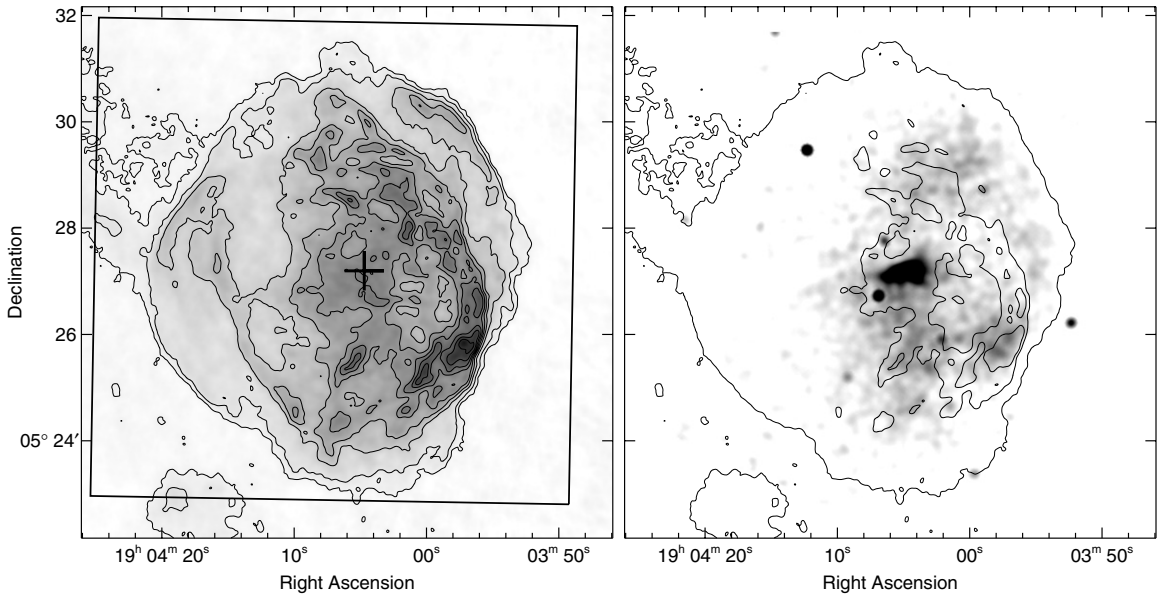

Figure 1. (Left) VLA 20 cm radio-continuum image of 3C 396 (Dyer & Reynolds 1999). The contour levels are 1, 2, 4, 8, 10, 12, 14, and 16 mJy beam^{-1} and the beam size is $6\farcs8 \times 6\farcs1$. The large box inside indicates the field covered by our NIR imaging observations with WIRC. The cross at the center marks the central position of its X-ray pulsar wind nebula. (Right) *Chandra* X-ray image of 3C 396 (Olbert et al. 2003) superimposed on radio contours of 1, 8, and 12 mJy beam^{-1}.

paper as follows. We first give a description of our NIR imaging and spectroscopic observations of 3C 396 in Section 2, together with the basic data reduction processes. In Sections 3 and 4, we present the results of the [Fe II] and H_2 line observations, respectively. We discuss the origin of the [Fe II] and H_2 emission in Section 5 and summarize the paper in Section 6.

2. OBSERVATIONS AND DATA REDUCTION

Near-IR narrowband imaging observations of the SNR 3C 396 were carried out to search for [Fe II] and H_2 emission using WIRC aboard the Palomar 5 m Hale telescope on 2005 July 15 and August 28 and 29. WIRC is equipped with a Rockwell Scientific now Teledyne Hawaii II HgCdTe 2K IR focal plane array, covering a $\sim 8\farcm5 \times 8\farcm5$ field of view with a $0\farcs25$ pixel scale. Our WIRC field covers the entire area of 3C 396 seen in radio except for a tiny portion of the faint tail in the east (see Figure 1). The narrowband filters for the 1.64 μm [Fe II] line and 2.12 μm H_2 line were used, together with *H*-cont and *K*-cont filters to subtract out continuum emission. The detailed observing parameters are given in Table 1. For the basic data reduction, the dark and sky background were subtracted out from each dithered frame using the median filtering of stacked dithered frames, and then the dithered frames were combined into a final image after flat fielding. The photometric solutions of the [Fe II] and H_2 images were obtained using the aperture photometry of 14 isolated stars from the Two Microns All-Sky Survey (2MASS) point source catalog (Skrutskie et al. 2006). The obtained instrumental magnitudes of the [Fe II] and H_2 images were found to have a very good correlation ($r \simeq 1$) with the 2MASS *H* and K_s magnitudes. Astrometric solutions were also obtained using the 2MASS stars. The 1-σ uncertainties of both R.A. and decl. directions in the [Fe II] and H_2 images were smaller than $0\farcs05$, which is within the systematic accuracy of the 2MASS astrometry.

The left panels in Figures 2 and 3 present the WIRC images obtained with the [Fe II] 1.64 μm and H_2 2.12 μm narrowband filters respectively, where we see filamentary nonstellar emission in both the [Fe II] and H_2 images, which are highly contaminated by the emission from numerous stars in the field. In order to see the nonstellar emission more clearly we subtracted out the stellar emission using the continuum emission images obtained with the *H*-cont and *K*-cont filters. For this we first performed point-spread function (PSF) photometry of the *H*-cont image to obtain a list of stars for continuum subtraction, and then subtracted out the corresponding stars in the [Fe II] image. To enhance the image quality we applied a median filtering with a square box of $1\farcs75 \times 1\farcs75$ and then smoothed the resulting image using a Gaussian with a $1''$ FWHM. It was difficult to remove several very bright stars with the above method, so we simply masked them out. We followed the same procedure with the H_2 and *K*-cont images. The right panels in Figures 2 and 3 present the star-subtracted images obtained with the [Fe II] and H_2 filters, and we can clearly identify the nonstellar extended emission in 3C 396. We give detailed analysis of the [Fe II] and H_2 emission in Sections 3 and 4.

After the aforementioned imaging observations, follow-up spectroscopic observations were carried out using the Long-slit Near-IR Spectrograph aboard the same Hale Telescope (Larkin et al. 1996). The spectrograph is equipped with a 256 × 256 HgCdTe NICMOS detector from Rockwell International now

Table 1
Parameters of WIRC Imaging Observations

Filter	λ_c[a]	$\Delta\lambda$[b]	Exposure[c]	Date
[Fe II]	1.644 μm	0.0252 μm	900 s	2005. 07. 15.
H_2	2.120 μm	0.0329 μm	600 s	2005. 08. 28.
H-cont	1.570 μm	0.0236 μm	300 s	2005. 08. 29.
K-cont	2.270 μm	0.0330 μm	300 s	2005. 08. 29.

Notes.
[a] The central wavelength of the filter obtained from http://www.astro.caltech.edu/palomar/200inch/WIRC/wirc_spec.html.
[b] Equivalent width of $\Delta\lambda = \int S(\lambda)d\lambda$ where $S(\lambda)$ is the normalized filter response.
[c] The integrated exposure over dithered frames of 30 s exposure.

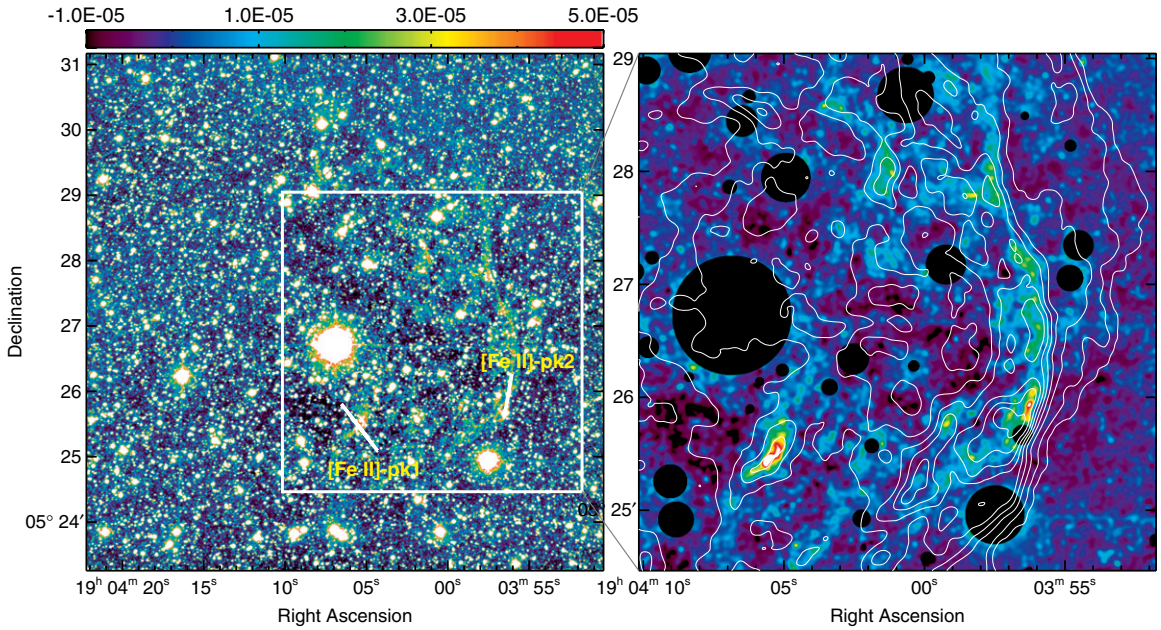

Figure 2. (Left) WIRC image of 3C 396 obtained with the [Fe II] 1.64 μm narrowband filter. The filamentary [Fe II] emission is detected in the western part of remnant distinguished from the pointlike stellar emission. The two slit positions used for the spectroscopic observations are indicated by elongated white bars in the small internal panel. The surface brightness scale range of two panel images is expressed by the color bar at the top in units of ergs cm^{-2} s^{-1} sr^{-1}. (Right) Enlarged image of the panel in the left after the subtraction of stellar emission, superimposed on radio contours. Median-box filtering and Gaussian smoothing are applied to enhance the image quality (see Section 2).

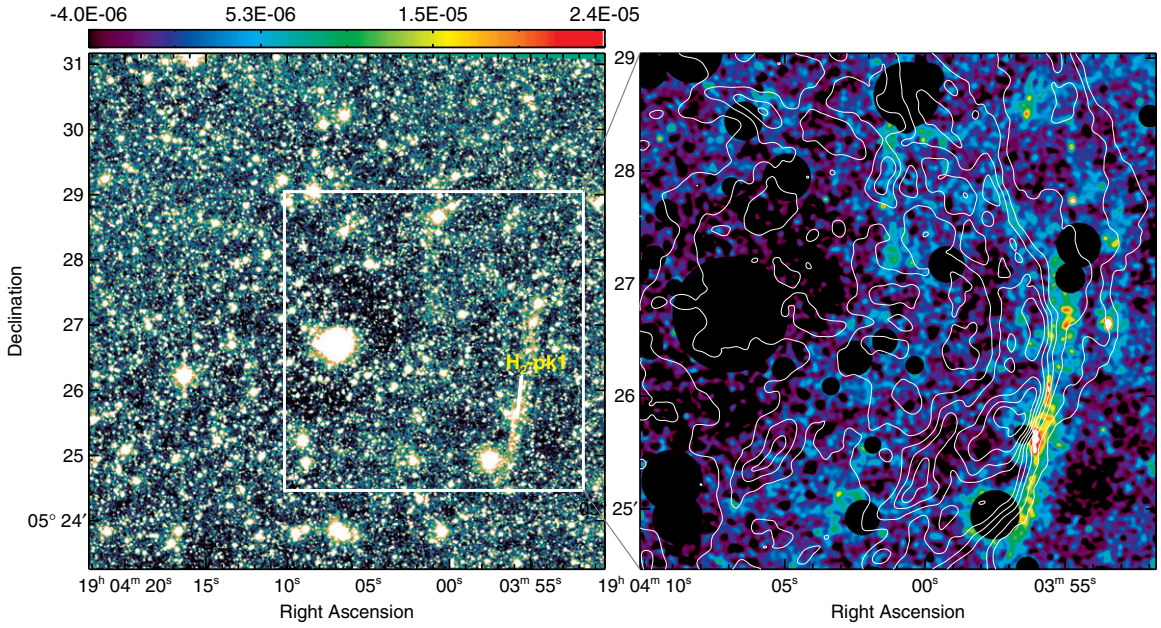

Figure 3. Same as Figure 2 but for the H_2 emission.

Teledyne, providing a 38″ slit length and 1″ (= 6 detector pixels) slit width. Both low-resolution ($R \simeq 700$) and high-resolution ($R \simeq 5000$) modes of the spectrograph were used for the observations. The spectral coverages of the low-resolution mode were $\sim$ 0.06 and 0.12 μm for the [Fe II] (1.64 μm) and H_2 (2.12 μm) lines respectively, while that of the high-resolution mode was $\sim$ 0.02 μm for the [Fe II] line. Note that only the [Fe II] line was observed with the high-resolution mode. The [Fe II] line spectra were obtained toward two bright peaks of the 1.64 μm [Fe II] line emission found in the WIRC image (see Section 3). The coordinates (J2000) of these two peaks, which are referred to as [Fe II]-pk1 and [Fe II]-pk2 in this paper, are (R.A., decl.) = ($19^h04^m05^s.54$, +05°25′26.″8) and ($19^h03^m56^s.29$, +05°25′56.″0), respectively. As in Figure 2 [Fe II]-pk1 is located inside 3C 396 while [Fe II]-pk2 is at its western boundary. The H_2 line spectrum was obtained toward the peak position at ($19^h03^m56^s.08$, +05°25′38.″3), which is referred to as H_2-pk1. The parameters of the spectroscopic observations are listed in Table 2. Both flat fielding and atmospheric opacity correction were performed by dividing the spectrum of a standard G-type star obtained at a similar airmass just after the target observations. Then the target spectrum was multiplied by a blackbody curve with an effective temperature of the standard G-type star. The OH air glow lines (Rousselot et al. 2000) were

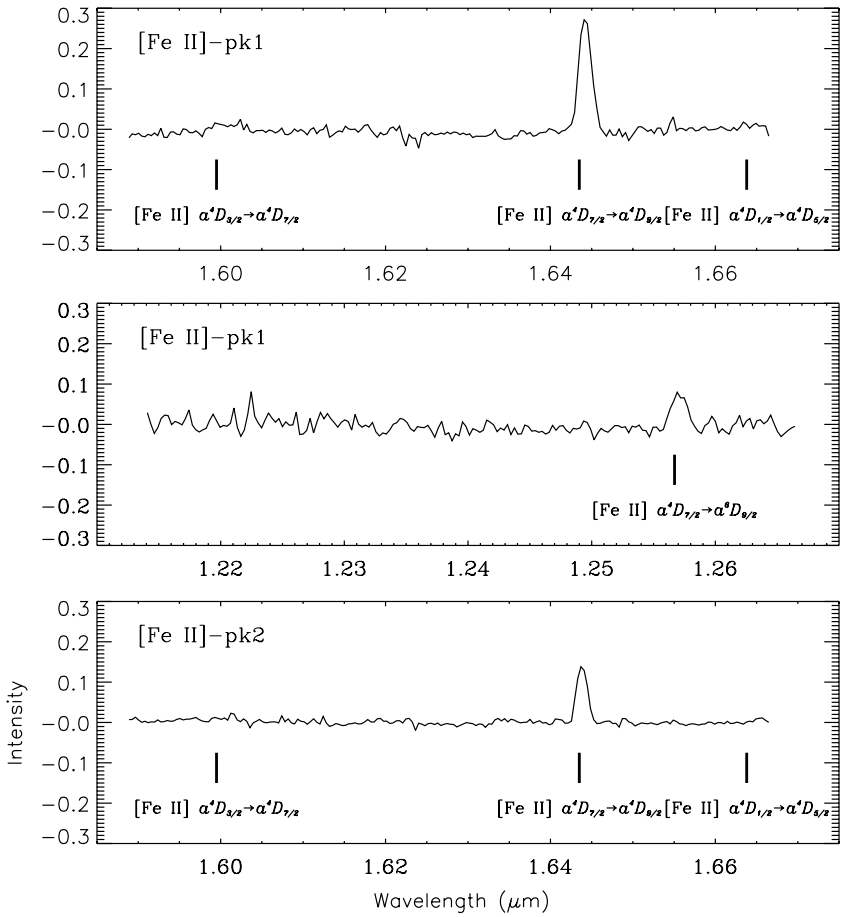

Figure 4. (Top) Low-resolution spectrum of the [Fe II] 1.64 μm line transition from [Fe II]-pk1. The air wavelengths of the [Fe II] transitions are indicated. (Middle) Same as the top panel, but for the [Fe II] 1.26 μm line transition. (Bottom) Same as the top panel, but for [Fe II]-pk2.

Table 2
Parameters of Spectroscopic Observations

Position	Central wavelength	Exposure	Mode[a]	Date
[Fe II]-pk1	1.24 μm	600 s	Low	2005. 08. 26.
	1.63 μm	600 s	Low	2005. 08. 26.
	1.64 μm	1200 s	High	2006. 06. 09.
[Fe II]-pk2	1.63 μm	300 s	Low	2005. 08. 26.
H_2-pk1	2.09 μm	300 s	Low	2006. 06. 10.

Note. [a] Low: low-resolution mode; High: high-resolution mode.

used for wavelength calibration and the Earth motion was corrected.

3. RESULTS OF [Fe II] OBSERVATIONS

3.1. Distribution of [Fe II] Emission in 3C 396

We can clearly identify extended, nonstellar [Fe II] emission spread over the central and the western parts of 3C 396 in Figure 2. The brightest [Fe II] emission is from the [Fe II]-pk1 knot, which is about $\sim 1'$ (or 2 pc) south from the center. Its surface brightness is $7.6 \pm 0.5 \times 10^{-5}$ ergs cm^{-2} s^{-1} sr^{-1}, and the $\sim 30''$ long (or 1 pc) northwest-southeast elongation matches the local radio emission well. In addition to the emission around the [Fe II]-pk1 knot, there is a long, curved, half ring-like [Fe II] filament in the western boundary of 3C 396. This filament, which peaks at [Fe II]-pk2, is clumpy and $\sim 3'$ (or 7 pc) long. Its peak and average surface brightnesses are $4.6 \pm 0.5 \times 10^{-5}$ and $1.5 \pm 0.5 \times 10^{-5}$ ergs cm^{-2} s^{-1} sr^{-1}, respectively. Compared to the radio emission, this filamentary [Fe II] emission is confined by radio contours delineating the inner edge of a large, bright half-shell feature prominent in radio in the western part of the remnant (Figures 1 and 2). The radio half-shell feature is relatively thick ($\sim 0.'5$ or 1 pc), and the brightnesses of both the [Fe II] and radio emission drop sharply across the western boundary of this feature. The central [Fe II] emission and the emission in the west appear to be connected through low surface brightness [Fe II] emission. There is also more diffuse [Fe II] emission in the north around (R.A., decl.) = ($19^h03^m58^s$, $+05°29'10''$), although it might be an extension of the filamentary emission in the west. The mean surface brightness of the emission in the north is $0.8 \pm 0.5 \times 10^{-5}$ ergs cm^{-2} s^{-1} sr^{-1}. Integrating all the features mentioned above, the total flux of the [Fe II] 1.64 μm emission in 3C 396 is $1.8 \pm 0.6 \times 10^{-12}$ erg cm^{-2} s^{-1}.

3.2. [Fe II] Spectroscopic Observations

3.2.1. Low-Resolution Spectroscopy

Figure 4 presents low-resolution spectra of [Fe II]-pk1 and [Fe II]-pk2. For [Fe II]-pk1, we placed the slit perpendicular to the elongation direction of the clump, while the slit direction was parallel to the direction of the filamentary emission for [Fe II]-pk2 (see Figure 2). We have averaged the extended emission over $\sim 5''$ (for [Fe II]-pk1) and $27''$ (for [Fe II]-pk2) regions around

Table 3
Relative Intensities of the [Fe II] and H_2 Lines

Position	Wavelength	Transition	Relative Strength	
			Observed	Dereddened
[Fe II]-pk1	1.26 μm	[Fe II] $a^4D_{7/2} \rightarrow a^6D_{9/2}$	0.232 (0.026)	1.05 (0.13)
	1.60 μm	[Fe II] $a^4D_{3/2} \rightarrow a^4F_{7/2}$	<0.034	<0.039
	1.64 μm	[Fe II] $a^4D_{7/2} \rightarrow a^4F_{9/2}$	1	1
	1.66 μm	[Fe II] $a^4D_{1/2} \rightarrow a^4F_{5/2}$	<0.028	<0.027
[Fe II]-pk2	1.60 μm	[Fe II] $a^4D_{3/2} \rightarrow a^4F_{7/2}$	<0.019	<0.022
	1.64 μm	[Fe II] $a^4D_{7/2} \rightarrow a^4F_{9/2}$	0.400 (0.014)	0.400 (0.014)
	1.66 μm	[Fe II] $a^4D_{1/2} \rightarrow a^4F_{5/2}$	<0.010	<0.009
H_2-pk	2.03 μm	H_2 1-0 S(2)	0.247 (0.081)	0.284 (0.093)
	2.07 μm	H_2 2-1 S(3)	<0.023	<0.025
	2.12 μm	H_2 1-0 S(1)	1	1

their peak emission to obtain the spectra. The NIR [Fe II] emission is known to have several other line transitions besides the transition at 1.64 μm, including the transitions at 1.26, 1.60, and 1.66 μm (e.g., Koo et al. 2007). We clearly detected the 1.64 μm transition from both [Fe II]-pk1 and [Fe II]-pk2, while we detected the 1.26 μm transition only from [Fe II]-pk1. Note that our [Fe II]-pk2 spectrum does not cover the 1.26 μm transition. For all other transitions we obtain the upper limits of their intensities relative to that of the 1.64 μm transition. Table 3 summarizes the results.

The [Fe II] 1.26 and 1.64 μm transitions originate from the same upper level. Thus their intensity ratio can provide information on the extinction toward the source, given the Einstein A coefficients. The exact values of the A coefficients, however, are somewhat controversial and their ratio could be from 1.04 (Quinet et al. 1996) to 1.49 (Smith & Hartigan 2006). From [Fe II]-pk1, we obtain [Fe II] 1.26 to 1.64 μm line ratio of 0.232 ± 0.026, which gives the visual extinction in the range of $A_V = 17 - 21$ mag based on the extinction cross section per hydrogen nuclei for the carbonaceous-silicate model of interstellar dust with $R_V = 3.1$ (Draine 2003). The estimated column density of hydrogen nuclei is $N_H = (3.4\text{–}4.2) \times 10^{22}$ cm^{-2}, which is between the values obtained by X-ray and radio H I observations (Becker & Helfand 1987; Harrus & Slane 1999; Olbert et al. 2003). We adopt $N_H = 3.4 \times 10^{22}$ cm^{-2}, which is approximately the middle value of X-ray and H I observations, in this paper. On the other hand, the intensity ratios of the two undetected [Fe II] transitions at 1.60 and 1.66 μm to the 1.64 μm transition is useful to estimate the upper limit of electron number density (e.g., Koo et al. 2007). We solve the rate equation of 16 levels of the ionized iron using the atomic parameters assembled by the CLOUDY program (version C05.05; Ferland 1998), and derive an upper limit of the electron number density to be $\lesssim 2000$ cm^{-3} for both [Fe II]-pk1 and [Fe II]-pk2 at an assumed temperature of 5000 K.

3.2.2. High-Resolution Spectroscopy

Figure 5 (top) is the high-resolution spectrum of [Fe II] 1.64 μm emission from [Fe II]-pk1 averaged over a 10″ area around the peak. The central velocity and the FWHM of the line are $v_{LSR} = +117 \pm 18$ km s^{-1} and 149 ± 5 km s^{-1}, respectively. For comparison, the velocity of [Fe II]-pk2 in the western boundary measured from the low-resolution spectrum in Figure 2 is $+50 \pm 26$ km s^{-1}, which is close to the systematic velocity +69 km s^{-1} of 3C 396 caused by the Galactic rotation (see Section 4.1). The large linewidth of the averaged spectrum is partly due to a velocity shift, which is apparent in the position–velocity diagram in Figure 5 (bottom) where we can identify a

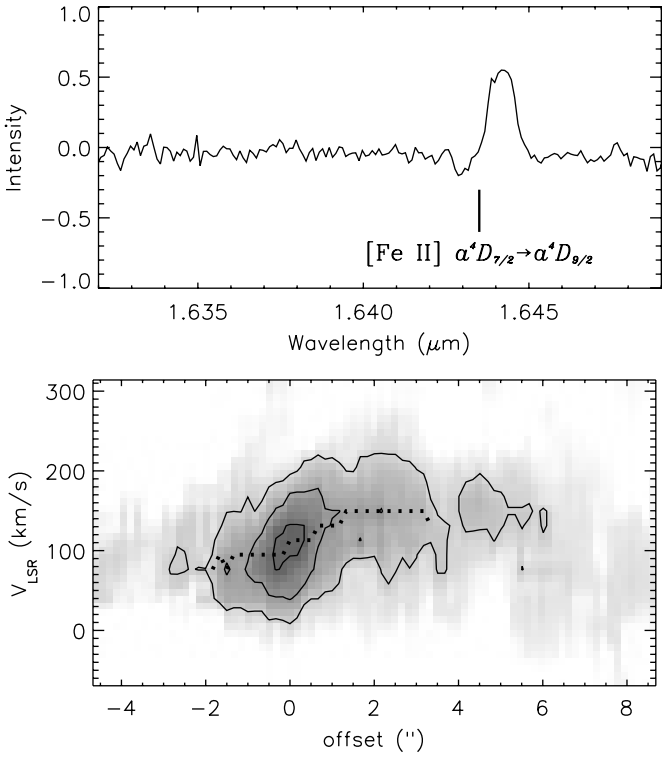

Figure 5. (Top) High-resolution spectrum of the [Fe II] 1.64 μm line transition from [Fe II]-pk1. Note that the center of the line profile is shifted from the rest wavelength of the transition indicated by the vertical line, clearly showing a Doppler shift. (Bottom) Position–velocity diagram of the high-resolution spectrum in the top panel. The dotted line represents the evolution of the velocity centroids along the offset. The negative offset corresponds to the northeast along the slit.

velocity shift from 93 to 145 km s^{-1} across the peak position from the northeast to the southwest direction. The measured velocity +117 km s^{-1} of [Fe II]-pk1 corresponds to a radial velocity of +48 km s^{-1} after subtraction of the contribution from the Galactic rotation.

If all the [Fe II] emission in 3C 396 is originated from the surface of an expanding sphere of 2.′5 (or 6 pc) radius, which is the average distance of the western filament from the center, then the three-dimensional expansion velocity of [Fe II]-pk1 is $\sim$ 56 km s^{-1}. Note that the radial velocity of the western filament is comparable to the systematic Galactic rotational velocity of 3C 396, indicating that the filament motion is largely transverse. The obtained expansion velocity of 56 km s^{-1} is too low to be ejecta (e.g., D.-S. Moon et al. 2009, in preparation), which suggests that the [Fe II] gas in 3C 396 is primarily the ambient or circumstellar gas swept up by the SNR shock. Generally

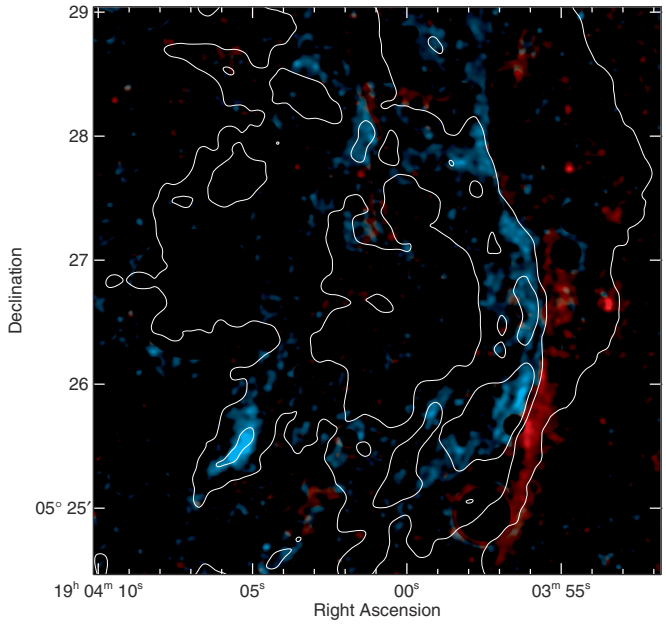

Figure 6. Comparison between the star-subtracted images of the [Fe II] and H_2 emission superimposed on the radio contours in the western boundary of 3C 396. Blue is for the [Fe II] emission; red is for the H_2 emission. Note that the H_2 emission is clearly located outside the [Fe II] emission from the center.

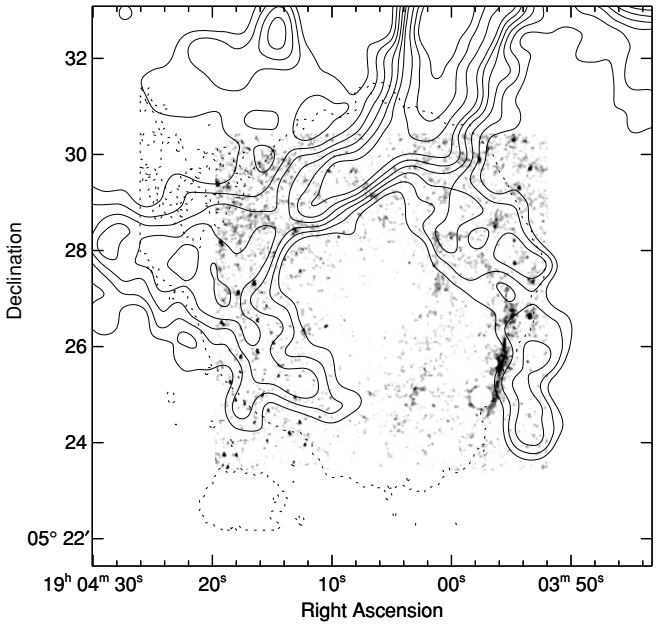

Figure 7. Comparison between the WIRC H_2 2.12 μm image of 3C 396 and contours of the ^{13}CO $J = 1$–0 transition integrated over the velocity range of 68–70 km s^{-1} (see the text). The radio-continuum boundary of the remnant is marked by dotted line.

the SNR shocks become radiative at expansion velocities of $<$200 km s^{-1} (McKee & Hollenbach 1980), so that the above expansion velocity of 56 km s^{-1} of 3C 396 appears to be consistent with the detection of the shocked [Fe II] lines in this remnant. In addition, the dereddened surface brightness ((0.1–1.2) $\times 10^{-3}$ ergs cm^{-2} s^{-1} sr^{-1}) can be explained by a shock propagating into the gas of $n_{\rm H} = 10^3$–10^4 cm^{-3} with a velocity of 30–50 km s^{-1} (Hartigan et al. 2004).

4. RESULTS OF H_2 OBSERVATIONS

4.1. Distribution of H_2 *Emission and Molecular Gas Toward 3C 396*

There is only one conspicuous feature in the H_2 2.12 μm emission which is a long ($\sim 3'$, or 7 pc) filamentary emission along the southwestern boundary of 3C 396 (Figure 3). The peak position (H_2-pk1) is slightly south of the position of [Fe II]-pk2, and its surface brightness is $2.4 \pm 0.2 \times 10^{-5}$ ergs cm^{-2} s^{-1} sr^{-1}. The total integrated flux of the H_2 2.12 μm emission is $4.1 \pm 1.3 \times 10^{-13}$ erg cm^{-2} s^{-1}. Figure 6 compares the relative locations of the [Fe II] and H_2 emission superimposed on the radio contours. It is apparent that the H_2 emission is located slightly farther than the [Fe II] emission from the SNR center, and the former is linear as opposed to the latter, which is curved along the bright radio emission. The [Fe II] and H_2 filaments are adjacent near the position of [Fe II]-pk1, but are apparently separated at the edges.

Across the southwest boundary of 3C 396, the radio emission drops sharply (Figure 1). This, together with our detection of the H_2 emission, strongly suggests that 3C 396 has encountered dense medium in this region, most likely a molecular cloud. In order to investigate this further we examined the distribution of molecular gas around 3C 396 using the Galactic Ring ^{13}CO $J = 1$–0 line Survey (Jackson et al. 2006) and found molecular gas at $v_{\rm LSR} = 68$–70 km s^{-1} surrounding 3C 396 (Figure 7). These velocities are consistent with the previously proposed systematic velocity of 3C 396 (Caswell et al. 1975), and the location of the H_2 filament that we found in this study matches the inner boundary of the molecular gas that forms a ring-like structure. Therefore, it is likely that 3C 396 is indeed interacting with some of these molecular clouds. If we adopt the velocity (69 km s^{-1}) of the molecular gas as the systemic velocity of 3C 396, its distance is 8.5 kpc, which we use in this paper as the distance to 3C 396.

4.2. Spectroscopic Observations and Molecular Shocks

Our H_2 spectrum of H_2-pk1 averaged over a 24″ area around the peak is shown in Figure 8. The H_2 2.12 μm 1–0 S(1) line stands out clearly, while the detection of H_2 2.03 μm 1–0 S(2) line is marginal. The H_2 2.07 μm 2–1 S(3) line is not detected, which could be partly due to the incomplete OH airglow subtraction. The ratio of the H_2 2.03 μm 1–0 S(2) line to the 2.12 μm 1–0 S(1) line is 0.25 ± 0.08, giving an excitation temperature of $T_{\rm ex} = 820 \pm 350$ K based on the transition probabilities of Wolniewicz et al. (1998) and an ortho-to-para hydrogen ratio of 3. This is lower than the general value of $\sim$ 2000 K derived from the rovibrational H_2 1–0 S(1) and 2–1 S(1) line ratios in thermalized molecular shock regions (Burton et al. 1989). It may be that in the case of 3C 396 the density of the molecular gas is smaller than the critical density for thermalization, so that the excitation temperature is lower.

The dereddened surface brightness of H_2-pk1 is 1.4×10^{-4} ergs cm^{-2} s^{-1} sr^{-1}. This surface brightness can be produced by a C shock penetrating into a molecular cloud of $n_H = 10^4$ cm^{-3} and $B = 50 - 100$ μG with a shock velocity of 20–30 km s^{-1} (Draine et al. 1983). Since we are observing tangentially to the shock front in 3C 396, the real density could be lower than the model value, which was calculated for a normal surface brightness.

5. ORIGIN OF THE [Fe II] AND H_2 FILAMENTS

We detected the [Fe II] 1.64 μm and H_2 2.12 μm filaments, which are close to each other in the western boundary of 3C 396. While the [Fe II] filament is curved and distributed along

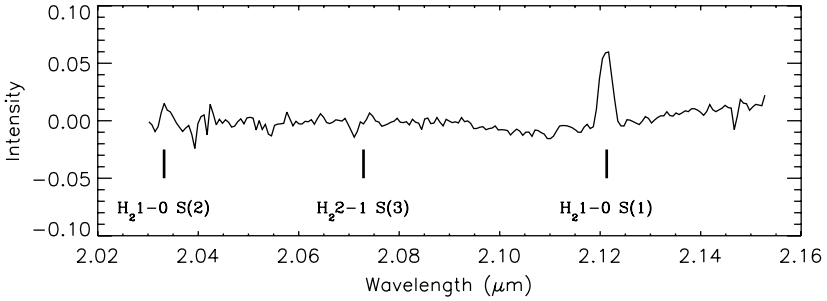

Figure 8. Low-resolution spectrum of H_2 2.12 μm transition from H_2-pk1. The air wavelengths of the H_2 transitions are indicated.

the bright radio emission, the H_2 filament appears to be straight and is located just *outside* the bright radio emission. The [Fe II] and H_2 filaments are adjacent in the middle, but are apparently separated at the edges. The former is brighter than the latter.

What would be the origin of these filaments? In principle, one can observe the emission from both Fe^+ ions and H_2 molecules in a single SNR shock if the shock is radiative and has swept up enough column density to have reformation of molecules behind the shock (e.g., Hollenbach & McKee 1989b). However, in such cases the H_2 emission originates in the downstream, which is opposite to the "reversal" of the relative positions between the [Fe II] and H_2 emission observed in 3C 396 (Figure 6). Interestingly 3C 396 is not the first SNR where the "reversal" is detected. It has been previously detected in several SNRs, including RCW 103 (Oliva et al. 1989, 1990), G11.2−0.3 (Koo et al. 2007), and W49B (Keohane et al. 2007). The "reversal" was also observed in W44 (Reach et al. 2005), but it is excluded in our discussion because it is an old SNR and also [Fe II] emission is fainter than H_2 emission, on the contrary to the other SNRs. Table 4 summarizes the properties of these four SNRs (including 3C 396) where we list their distances, radii, and ages, along with their interactions with ambient molecular clouds. For the origin of the "reversal" between the NIR [Fe II] and H_2 emission, Oliva et al. (1990) considered the excitation of H_2 by ultraviolet or X-rays from an SNR, although it appears unlikely because of the difficulty in exciting the cold gas. For W49B, Keohane et al. (2007) proposed an explosion inside a wind bubble within a molecular cloud and H_2 emission being produced by a "jet" propagating beyond the bubble; however, it is inadequate to explain all the four SNRs.

All the SNRs in Table 4 are core-collapse SNRs with relatively small radius of $\lesssim$ 10 pc. According to Chevalier (2005), G11.2−0.3 and RCW 103 are remnants of Type IIL/b SNe that had intermediate-mass (25–35 $M_\odot$) progenitors with strong red supergiant (RSG) winds, and the SNR shocks are interacting with the wind material extending to 5–7 pc. The radio morphology of 3C 396, together with the detection of [Fe II] and H_2 filaments, indicates that it may also be a remnant of a Type IIL/b SN. In the radio emission (Figure 1), there exists a thick, half ring-like bright radio shell (BRS) in the western part of the remnant. Beyond this BRS of $\sim 2\farcm5$ (or 6 pc) radius, there appears faint plateau-like emission especially in the north and south of the remnant. We interpret this BRS as the RSG wind material confined by the ambient pressure and the faint extended plateau-like emission as originating from the SNR shock that has crossed the boundary of the wind material. This interpretation is consistent with the size of the BRS, which is comparable to to the typical size of the RSG wind material confined by the ambient pressure (Chevalier 2005). In this scenario, the [Fe II] emission may trace the shocked material of the RSG wind, while the H_2 emission may represent interactions between the SNR shock and a wind-blown bubble produced during the main sequence (MS) phase of the progenitor star by its fast stellar winds (e.g., McKee et al. 1984b). This also provides a natural explanation of the positional "reversal" between the [Fe II] and H_2 emission. The H_2 filament could be either the inner boundary of the MS wind-blown bubble or molecular clumps left over inside the bubble. We note that the 4.5 and 5.8 μm emission of 3C 396 detected with *Spitzer* (Lee 2005; Reach et al. 2006; see Section 1) can also be explained by this scenario. The *Spitzer* 4.5 μm waveband contains the wavelengths of pure rotational H_2 lines, while the 5.8 μm one does those of many atomic lines, including the [Fe II] line at 5.34 μm. The 4.5 μm emission is located slightly outside of the 5.8 μm emission, consistent with what we see in this study with the NIR H_2 and [Fe II] line emission. In conclusion, the two-stage SNR shock interactions with RSG wind material and also with a MS wind-blown bubble appear to explain the NIR [Fe II] and H_2 emission in the young SNRs of Type IIL/b SNe, including 3C 396.

We suggest that the [Fe II] emission in 3C 396 represent dense clumps in the RSG wind of the progenitor star as follows. The expansion velocity of [Fe II]-pk1 is very small compared to what we expect from a young SNR. If we use the hot gas temperature of 0.62 keV derived from X-ray observations (Harrus & Slane 1999), the implied velocity of the SNR shock in 3C 396 is in fact 600 km s^{-1}. This discrepancy indicates that the ambient medium may be inhomogeneous, so that the SNR shocks propagating into dense clumps are slow and radiative while the shocks propagating through the diffuse interclump medium are fast and nonradiative. Generally in a shocked gas the [Fe II] lines are emitted in the far downstream where hydrogen atoms are mostly neutral at $T = 10^3$–10^4 K (McKee et al. 1984a; Hollenbach et al. 1989a; Oliva et al. 1989). This is because the ionization potential of the Fe atom is low (7.9 eV) and the far-ultraviolet photons from hot shocked gas can penetrate far downstream to maintain the ionization state of Fe^+. The upper limit of the electron density that we derived in Section 3.2.1 gives an upper limit of the density of hydrogen nuclei $n_H \approx n_e/0.11 \lesssim 2 \times 10^4$ cm^{-3} if the mean ionization fraction is 0.11 (Oliva et al. 1989). Assuming 5000 K as the temperature of the [Fe II] line emitting region, the thermal pressure is $p/k_B \lesssim 1 \times 10^8$ cm^{-3} K where k_B is the Boltzmann constant, which is comparable to the thermal pressure of the X-ray emitting hot gas (Harrus & Slane 1999). This indicates that the shock in the [Fe II] gas can be driven by the thermal pressure of the hot gas. The preshock density may be estimated from $n_0 \approx p/\mu_H v_s^2 \sim 50$ cm^{-3} where μ_H ($= 2.34 \times 10^{-24}$ g) is the mean mass per hydrogen nuclei including the cosmic abundance of He and $v_s \simeq 56$ km s^{-1} is the shock speed. The density of the RSG wind at $r = 6$ pc is $n_w = \dot{M}/4\pi r^2 \mu_H v_w \sim 1$ cm^{-3} if we use the mass loss rate $\dot{M} = 5 \times 10^{-5}$ $M_\odot$ yr^{-1} and the wind speed $v_w = 15$ km s^{-1} (e.g., Chevalier 2005). Therefore, the preshock density of the

Table 4
Properties of SNRs with [Fe II] Inside H_2 Emission

Name	Distance (kpc)	Radius (pc)	Age (yrs)	SN Type	MC[a]	References
G11.2-0.3	5	3.3	1600	IIL/b	No	Koo et al. (2007)
RCW 103	3.8	5.0	2000	IIL/b	Yes	Oliva et al. (1990, 1999); Paron et al. (2006)
W49B	11.4	7	4000	...	No	Keohane et al. (2007)
3C 396	8.5	10	6000	IIL/b	Yes	This work

Note. [a] Detection of an ambient molecular cloud interacting with the SNR.

[Fe II] emitting gas is an order of magnitude greater than the mean density of the RSG wind, suggesting that the former represents dense clumps in the RSG wind material.

6. CONCLUSION

Stars of intermediate mass (25–35 $M_\odot$) have fast winds in the MS phase and slow dense winds during the RSG phase. Just before a core-collapse SN explosion, therefore, they are surrounded by a dense circumsteller region of 5–7 pc radius created by the RSG winds embedded within a low-density bubble produced by the MS winds (Chevalier 2005). Once it explodes, the SN shock encounters these pre-existing structures to generate in principle a multishell structure (e.g., Dwarkadas 2005), although the details can differ from case to case depending on the distribution of the interstellar medium. In this paper, based on the detection of the NIR [Fe II] and H_2 filaments, we propose that the SNR 3C 396 is a remnant of a Type IIL/b SN that shows such a multishell structure produced by the interactions of the SNR shocks with the RSG wind material (i.e., [Fe II] filament) and also with the MS wind-blown bubble (i.e., H_2 filament). This scenario can provide a natural explanation of the relative locations between the [Fe II] and H_2 emission, where the latter is placed farther from the center of the remnant than the former, and is also consistent with the *Spitzer* 4.5 and 5.8 μm emission of 3C 396. The [Fe II] emission likely represents dense clumps driven by the thermal pressure of hot X-ray emitting gas in the remnant. We identify that there exists a molecular cloud that appears to surround 3C 396. The velocities of the molecular gas are very similar to the systematic velocity of 3C 396, indicating that this molecular gas may be indeed interacting with 3C 396 to produce the H_2 emission. Further sensitive molecular line observations are needed to investigate this possibility more. Finally, we note that there are three other SNRs having [Fe II] and H_2 emission somewhat similar to that of 3C 396. We expect that these SNRs are also remnants of Type IIL/b SNe (e.g., Chevalier 2005) that have comparable environments produced by stellar winds of similar progenitors.

We thank Kristy Dyer for providing the VLA image of 3C 396. This work was partly supported by the Korea Science and Engineering Foundation through the Joint Research Project under the KOSEF-NSERC Cooperative Program (F01-2007-000-10048-0). D.-S.M. acknowledges the support from the Discovery Grant (327277) of Natural Science and Engineering Research Council of Canada.

Facility: Hale (WIRC, HNA)

REFERENCES

Anderson, M. C., & Rudnick, L. 1993, ApJ, 408, 514
Becker, R. H., & Helfand, D. J. 1987, AJ, 94, 1629
Burton, M. G., Brand, P. W. J. L., Geballe, T. R., & Webster, A. S. 1989, MNRAS, 236, 409
Caswell, J. L., Murray, J. D., Roger, R. S., Cole, D. J., & Cooke, D. J. 1975, A&A, 45, 239
Chevalier, R. A. 2005, ApJ, 619, 839
Draine, B. T. 2003, ApJ, 598, 1017
Draine, B. T., Roberge, W. G., & Dalgarno, A. 1983, ApJ, 264, 485
Dwarkadas, V. V. 2005, ApJ, 630, 892
Dyer, K. K., & Reynolds, S. P. 1999, ApJ, 526, 365
Ferland, G. J., Korista, K. T., Verner, D. A., Ferguson, J. W., Kingdon, J. B., & Verner, E. M. 1998, PASP, 110, 761
Green, D. A. 1989, MNRAS, 238, 737
Greenhouse, M. A., Woodward, C. E., Thronson, H. A., Rudy, R. J., Rossano, G. S., Erwin, P., & Puetter, R. C. 1991, ApJ, 383, 164
Harrus, I. M., & Slane, P. O. 1999, ApJ, 516, 811
Hartigan, P., Raymond, J., & Pierson, R. 2004, ApJ, 614, L69
Hollenbach, D., Chernoff, D. F., & McKee, C. F. 1989a, in Proc. of the 22nd Eslab Symp., ed. B. H. Kaldeich (ESA SP-290; Paris: European Space Agency), 245
Hollenbach, D., & McKee, C. F. 1989b, ApJ, 342, 306
Jackson, J. M., et al. 2006, ApJS, 163, 145
Keohane, J. W., Reach, W. T., Rho, J., & Jarrett, T. H. 2007, ApJ, 654, 938
Koo, B.-C., Moon, D.-S., Lee, H.-G., Lee, J.-J., & Matthews, K. 2007, ApJ, 657, 308
Larkin, J. E., Knop, R. A., Lin, S., Matthews, K., & Soifer, B. T. 1996, PASP, 108, 211
Lee, H.-G. 2005, JKAS, 38, 385
McKee, C. F., Chernoff, D. F., & Hollenbach, D. J. 1984a, in Galactic and Extragalactic Infrared Spectroscopy, ed. M. F. Kessler & J. P. Phillips (Dordrecht: Reidel), 103
McKee, C. F., & Hollenbach, D. J. 1980, ARA&A, 18, 219
McKee, C. F., van Buren, D., & Lazareff, B. 1984b, ApJ, 278, L115
Mouri, H., Kawara, K., & Taniguchi, Y. 2000, ApJ, 528, 186
Olbert, C. M., Keohane, J. W., Arnaud, K. A., Dyer, K. K., Reynolds, S. P., & Safi-Harb, S. 2003, ApJ, 592, L45
Oliva, E., Moorwood, A. F. M., & Danziger, I. J. 1989, A&A, 214, 307
Oliva, E., Moorwood, A. F. M., & Danziger, I. J. 1990, A&A, 240, 453
Oliva, E., Moorwood, A. F. M., Drapatz, S., Lutz, D., & Sturm, E. 1999, A&A, 343, 943
Paron, S. A., Reynoso, E., Purcell, C., Dubner, G. M., & Green, A. 2006, PASA, 23, 69
Quinet, P., Le Dourneuf, M., & Zeippen, C. J. 1996, A&AS, 120, 361
Reach, W. T., Rho, J., & Jarrett, T. H. 2005, ApJ, 618, 297
Reach, W. T., Rho, J., Jarrett, T. H., & Lagage, P.-O. 2002, ApJ, 564, 302
Reach, W. T., et al. 2006, AJ, 131, 1479
Rousselot, P., Lidman, C., Cuby, J.-G., Moreels, G., & Monnet, G. 2000, A&A, 354, 1134
Skrutskie, M. F., et al. 2006, AJ, 131, 1163
Smith, N., & Hartigan, P. 2006, ApJ, 638, 1045
Wolniewicz, L., Simbotin, I., & Dalgarno, A. 1998, ApJS, 115, 293